Constructing interface chemical coupling S-scheme heterojunction MoO$_{3-x}$@PPy for enhancing photocatalytic oxidative desulfurization performance: Adjusting LSPR effect via oxygen vacancy engineering

Chenchao Hu [a],[1], Jie Yin [c],[1], Suhang Xun [a],[e],*, Linhua Zhu [b],**, Hongping Li [c], Minqiang He [c], Peiwen Wu [c], Huaming Li [c], Wenshuai Zhu [c],[d],***

[a] School of Environment and Safety Engineering, Jiangsu University, Zhenjiang 212013, PR China
[b] Engineering Research Center of Tropical Marine Functional Polymer Materials of Hainan Province, Key Laboratory of Water Pollution Treatment and Resource Reuse of Hainan Province, Key Laboratory of Functional Organic Polymers of Haikou, College of Chemistry and Chemical Engineering, Hainan Normal University, Haikou 571158, PR China
[c] Institute for Energy Research, School of Chemistry and Chemical Engineering, Jiangsu University, Zhenjiang 212013, PR China
[d] College of Chemical Engineering and Environment, State Key Laboratory of Heavy Oil Processing, China University of Petroleum-Beijing, Beijing 102249, PR China
[e] Jiangsu Collaborative Innovation Center of Technology and Material of Water Treatment, Suzhou University of Science and Technology, Suzhou 215009, PR China

ARTICLE INFO

ABSTRACT

Construction of photocatalyst that combines excellent electron transfer and photoresponse capabilities to enhance photocatalytic performance remains a challenging task. In this work, interfacial Mo-N bonds and vacancy engineering collaborative modified MoO$_{3-x}$@polypyrrole (MP) S-scheme heterojunction is rational designed for efficient photocatalytic oxidative desulfurization. The addition of polypyrrole introduces rich defects which inducing the localized surface plasmon resonance (LSPR) effect and enhancing light absorption. Furthermore, the combination facilitates the formation of Mo-N bonds. The modifications amplify the built-in electric field and conduct the efficacious separation of photogenerated carriers. With the synergism of LSPR effect and interfacial chemical Mo-N bonds, the optimal MP photocatalyst displays attractive desulfurization rate of 100% for dibenzothiophene (DBT) in 60 min under illumination, touching the objective of ultra-deep desulfurization. The study extends a novel understanding of the impact of LSPR effect and heterojunction interface charge transfer on the photocatalytic desulfurization ability.

1. Introduction

Air pollution caused by sulfur oxides poses significant hazard to the environment and human health. The emission of sulfur compounds from fuel is major source of sulfur oxide in the air atmosphere [1]. Therefore, the production of "green fuel" and "low sulfur fuel" (S-content < 10 ppm) is an inevitable challenge in reducing the air pollution [2,3]. As the most traditional used desulfurization technology in the industry, hydro-desulfurization (HDS) extremely removes a substantial part of sulfur compounds in the oil [4]. However, the remove of heterocyclic aromatic sulfur compounds, like dibenzothiophenes (DBT) and its derivatives, requires stringent condition and is often accompanied by significant

economic costs [5]. To achieve deep desulfurization of oil and meet the standards of clean fuel, the development of efficient non-HDS technologies is indispensable [6–10]. In recent years, photocatalytic oxidative desulfurization (PODS) has been subjected to widespread concern as a low-energy, low-cost and high-efficiency desulfurization technology [11]. Based on the high demand for PODS process, a green and efficient oxidant involves to be pursued. Hydrogen peroxide (H$_2$O$_2$) has been particularly sought after due to its low economic costs and environmental pollution risks [12]. Under the action of photocatalysts and oxidant, photoexcitation often leads to the conversion of DBT and its derivatives to dibenzothiophene sulfone (DBTO$_2$) and other corresponding sulfone substances, which can be further extracted and

recovered due to the added value [13]. Therefore, the development and preparation of efficient photocatalysts are crucial for achieving photocatalytic oxidative desulfurization.

Non-precious metals-base plasmonic nanomaterials have drawn widespread attention in the field of photocatalytic results from their localized surface plasmon resonance (LSPR) effects, which often contributes to higher photochemical conversion efficiency compared to conventional semiconductor metal oxides [14–16]. The LSPR effect enhanced materials exhibit outstanding light absorption capacity and broadened spectral response range even extending to the spectrum absorption of near-infrared (NIR), as a result of the collective resonance of abundant free carriers on their surfaces when exposed to light within certain wavelength [17]. Huang et al. expanded the photoresponsive range of metallic tungsten carbide (WC) to the NIR region, achieving high efficiency in photocatalytic degradation of organic pollutants by enhancing the LSPR effect [18]. Consequently, the intensity of LSPR is heavily influenced by the surface free carrier density, which can be effectively increased by introducing oxygen defect sites on the catalyst surfaces and strengthen the photocatalytic performance [19]. Furthermore, previous research has demonstrated that the introduction of appropriate oxygen vacancies not only adjusts the electron structure, but also facilitates charge transfer and acts as an effective electron trap, thereby promoting the separation of photogenerated e^--h^+ [20]. Therefore, the enhanced LSPR effect by introducing more oxygen vacancies may contribute to the efficiency of photocatalysts for fuel desulfurization.

Non-stoichiometric molybdenum oxide (MoO_{3-x}), a non-precious metals-based plasmonic nanomaterial, has gained high attention due to its low cost, non-toxicity, abundant surface oxygen defect sites and strong LSPR effects [21]. The application of MoO_{3-x} has been reported in various fields such as hydrogen peroxide sensing, photocatalytic antibacterial activity and photocatalytic degradation of organic contaminant. Nevertheless, despite MoO_{3-x} is provided with excellent light absorption ability, the wide bandgap and speedy recombination of photogenerated e^--h^+ frequently limit its application as a single photocatalyst. Yang et al. achieved efficient photocatalytic disinfection of harmful bacteria by constructing a MoO_{3-x}/S-CN heterojunction, effectively modulating the electronic structure of MoO_{3-x} [22]. Wang et al. developed polydopamine-coated MoO_{3-x} and controlled its LSPR range, enhancing the detection efficiency of dyes by the synthesized material [23]. On the other hand, it is desirable to establish an electron channel to accelerate charge migration and force the movement of photogenerated e^- and h^+ to different directions with the driven of built-in electron filed (*E*-filed), which suppressing the recombination of e^--h^+ pairs and improving the electronic structure of the photocatalyst. As an organic semiconductor, polypyrrole (PPy) has aroused widespread interest because of the superior electronic transmission capability and structural plasticity [24]. The excellent photophysical property and well-matched bandgap of PPy make it an ideal component to photocatalytic modification as a composite material. However, the rational engineering of the interface with organic semiconductor to upgrade the electronic structure properties and photocatalytic performance still remains a daunting task.

Therefore, in this study, we structured vacancy engineering to induce LSPR effects which enhanced the utilization of sunlight, and further improved the electronic structure of the photocatalyst by combining with conductive polymer PPy. A series of MoO_{3-x}@PPy (MP) heterojunction catalysts with rich oxygen vacancies were prepared via one-pot in-situ polymerization method, forming Mo-N bonds as the electron transfer channel and efficiently accelerating the charge transfer between MoO_{3-x} and PPy. Furthermore, the mechanism of Mo-N bonds formation was explored through density function theory (DFT) calculations. The result showed that MP heterojunction photocatalyst possessed abundant LSPR effect and excellent photogenerated electron hole separation efficiency. The photocatalytic desulfurization performance was investigated in an extraction and photocatalytic oxidative desulfurization (EPODS) system taking for methyl cyanide (MeCN) as an extractant. The

prepared MP photocatalyst displayed outstanding photocatalytic desulfurization performance and realized the deep desulfurization within five cycles. Ultimately, the active free radicals (•OH and h^+) and reaction product ($DBTO_2$) in EPODS system were discussed and a possible mechanism was proposed.

2. Experimental

2.1. Materials

The necessary materials for the experiment and synthesis method of the samples are reflected in the Supplementary material.

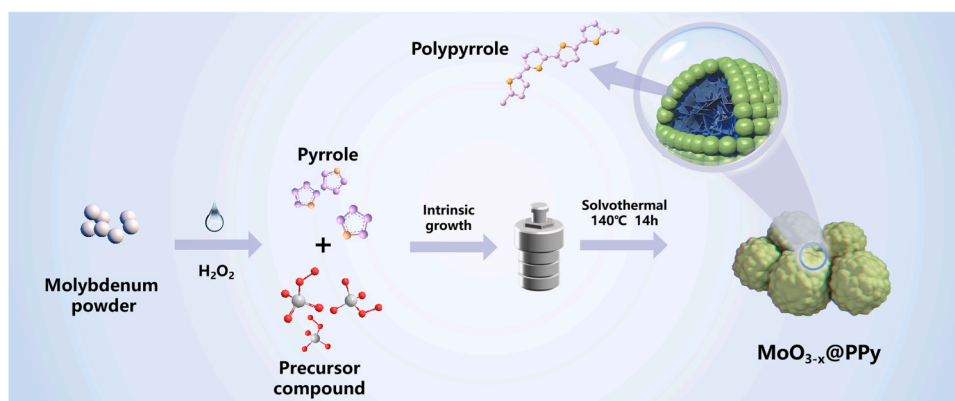### 2.2. Preparation of MoO_{3-x} nanosheets

According to a typical preparation strategy, the MoO_{3-x} nanosheets were obtained [25]. First, molybdenum metal powder (0.2 g) was joined into 1-butanol (24 mL) and ultrasonic dispersion for 20 min. Then 3 mL of H_2O_2 was introduced drop wise and continued stirring for 30 min until the transparent yellow solution was obtained, which generated the precursor of $MoO_2(OH)(OOH)$ [8]. The final mixture was carried on hydrothermal in reactor under 140 ºC sustaining 14 h. The precipitation after reaction was purified three times by deionization water and anhydrous ethanol and then vacuum dried under 60 ºC for 12 h. Ultimately, the blue solid powder is obtained after grinding.

2.3. Preparation of MoO_{3-x}@PPy (MP) heterojunction

As shown in Scheme 1, the preparation procedure of the MoO_{3-x}@PPy composite is basically analogous to that of MoO_{3-x}, the difference is that PPy is introduced into the system. Appropriate amount of pyrrole units was added in 10 mL of ethanol with ultrasonic dispersion as a pyrrole solution. On the other hand, 0.2 g molybdenum metal powder was added to 24 mL of 1-butanol and ultrasonic dispersion for 20 min. 3 mL of H_2O_2 was dripped slowly into and continue to stir for 30 min till the transparent yellow solution was obtained. Then the pyrrole solution was introduced to the transparent yellow solution slowly and magnetic stirred for 12 h to polymerize pyrrole adequately. After that, the mixture was transferred into a hydrothermal reactor and heated at 140 ºC for 14 h. The sediment obtained after hydrothermal treatment was purified three times by deionized water and anhydrous ethanol, finally drying under 60 ºC overnight. A series of catalysts were prepared by controlling the amount of pyrrole dosage, named MP-1 (62.5 μL), MP-2 (125 μL) and MP-3 (250 μL).

2.4. EPODS measurements

The EPODS tests were conducted using a photochemical reaction instrument GHX-3. The instrument is composed of 250 W xenon lamp, circulating cooling water device, 100 mL glass reactor and magnetic stirrer. In this research, DBT (dibenzothiophene), 4-MDBT (4-methyldibenzothiophene) and 4,6-DMDBT (4,6-dimethyldibenzothiophene) were dissolved in dodecane with 200 ppm sulfur content to prepare varying model oil, respectively, and hexadecane was added as an internal standard. To improve the dispersion of the photocatalysts, 0.03 g of prepared photocatalyst and 10 mL of model oil were added to the reactor, after that, followed by the addition of 5 mL methyl cyanide (MeCN) as an extractant. The temperature of the reactor was maintained at room temperature (25 ºC) by circulating condensate water. Initially, the multiphase mixture was stirred vigorously outside illumination lasting for half an hour to establish an extractive equilibrium. Subsequently, the moderate amount of H_2O_2 was rapidly introduced to the mixture keeping stirring. Then switched on the xenon lamp and clean oil was acquired every 15 min for remaining sulfur concentration analysis utilizing gas chromatography. Repeat each test three times to ensure high accuracy. The used catalysts were washed multiple times by CH_2Cl_2

Scheme 1. The preparation process of MoO$_{3-x}$@PPy.

and stoved under 60 °C in a vacuum state oven for 12 h and recycled for further operation. The desulfurization rate (η) was estimated via following formula:

$$\eta = \frac{C_0 - C_t}{C_0} \times 100\% \tag{1}$$

Where C_0 represents initial concentration of sulfur compounds of the mixture before the reaction, and C_t means residual concentration of S-compound content at time t (min).

2.5. Computational details

All the geometry optimization and DFT calculation in this research were accomplished by Gaussian 16 [26]. Owing to the sufficiently precise dispersion correction, the hybrid function B3LYP plays unique role in providing credible results for the most system [27]. The description of the electron wave function of H, C, N and O elements are given by 6–31 G(d) basis set and the Mo atoms is used for Stuttgart/Dresden (SDD) pseudo-potential basis set. The interaction energy between PPy and MoO$_{3-x}$ (MoO$_3$) is calculated by the Eq. (2). The convergence criteria

for the total energy is 1.0×10^{-8} a.u. ($\approx 6.3 \times 10^{-6}$ kcal•mol^{-1}), and the maximum force and maximum displacement of elements were set to 0.000063 a.u. and 0.0016 a.u. for the geometry optimization, respectively.

$$E_{\text{int}} = E_{MP} - E_{MoO_{3-x}}(E_{MoO_3}) - E_{PPy} \tag{2}$$

Where *EMP* indicates to the energy of MP composite. E_{MoO3-x}, E_{MoO3} and E_{PPy} express the energy of MoO$_{3-x}$ (Fig. S1(a)), E_{MoO3} (Fig. S1(b)) and PPy (Fig. S1(c)) monomers, respectively.

3. Results and discussion

3.1. Morphology and composition of photocatalysts

The typical synthetic route of MoO$_{3-x}$@PPy composite was illustrated in Scheme 1. It is widely acknowledged that transition-metal oxygen anionic exhibits well performance to initiate the oxidation and polymerization of organic polymer monomers [28].H$_2$O$_2$ and precursor MoO$_2$(OH)(OOH) generating by the reaction of Mo powder were rendered as ideal initiators for the polymerization of pyrrole.
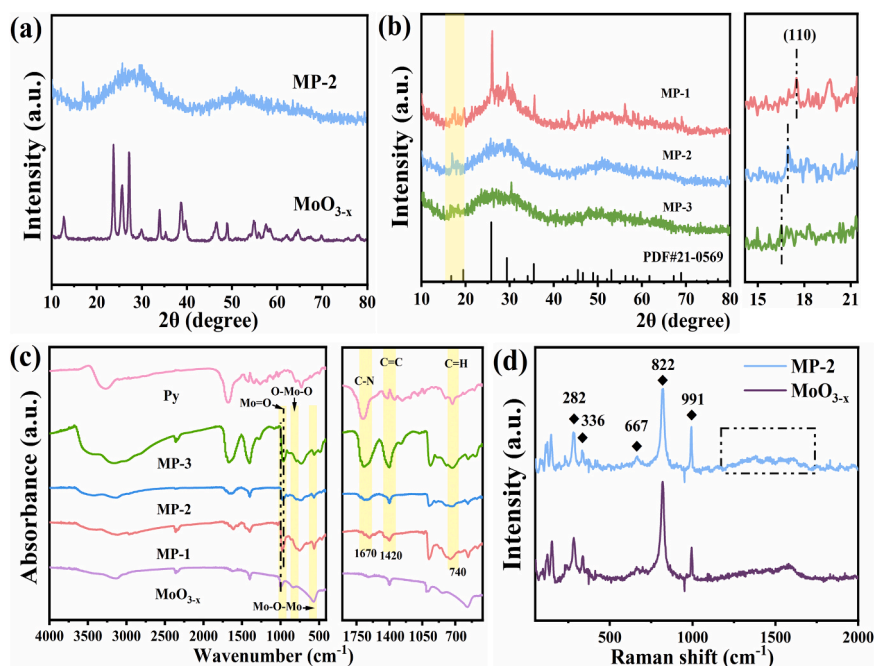

Fig. 1. XRD patterns of pure MoO$_{3-x}$ and composited photocatalyst (a), prepared photocatalysts with different amount of PPy (b); FT-IR spectra of the samples (c); Raman spectra of pure MoO$_{3-x}$ and MP-2 (d).

Furthermore, the unoccupied 4d orbital of Mo atoms from MoO_{3-x} can combine with the lone pair electrons on N atoms of pyrrole and establish covalent $Mo(\delta^+)-N(\delta^-)$ bonds [29,30]. These reactions tightly bind the interface between MoO_{3-x} and PPy. From the XRD analysis in Fig. 1(a), the prepared pure MoO_{3-x} was assigned to the orthorhombic phase and the photocatalyst showed phase transition to the hexagonal phase with the introduction of PPy. The corresponding diffraction of hexagonal phase was obviously observed in the XRD pattern of MP-1 when the added pyrrole was controlled in a fewer amount. However, the intensity of characteristic peaks weakened and diffraction of (210) plane at 26.1° disappeared as the further increase of pyrrole dosage (Fig. 1(b)). The phenomenon may be attributed to hindrance of advantageous planar growth caused by the electrostatic adsorption of PPy by MoO_{3-x} surface during the synthesis process. Moreover, a slightly shifted angle at the peak of 16.8° can be observed, corresponding the interplanar spacing of (110) crystal plane of MoO_{3-x} continuously expanding with the larger amount of PPy. The occurrence of the phenomenon can be ascribed to the incorporation of N atoms with greater radius than that of O atoms and the interaction which formed by construction of heterojunction interface between MoO_{3-x} and PPy [31]. Significantly, according to the relevant research, the lattice deformation is beneficial for the formation of oxygen vacancies [32].

The element bonding and functional groups of synthesized catalyst was considered though FT-IR spectra in Fig. 1(c). For pure MoO_{3-x} and all the MP composites, peaks at 575 and 842 cm^{-1} were observed, attributing to the symmetric and dissymmetric stretching vibrations of Mo-O-Mo [33]. Additionally, a peak located at 985 cm^{-1} was present, arising from the stretching vibration of Mo=O [34]. Notably, a slight blue shift of the M=O peak can be observed with the introduction of pyrrole, demonstrating that the occurrence of interactivity between molybdenum oxide and PPy. At the same time, characteristic peaks for pyrrole were also identified in FT-IR spectrum. The peaks located in 1670, 1543 and 740 cm^{-1} were resulted from bending vibrations of the C-N, C=C and C-H bonds on pyrrole ring, respectively [6]. The blue shift of the C-N bond with the addition of PPy might due to the formation of interforce between the lone pair electron of N atoms on pyrrole and the defect state on the MoO_{3-x} surface [35]. Besides that, Raman

spectroscopy was performed on the catalyst before and after PPy complexation. As displayed in Fig. 1(d), peaks corresponding to the Mo-O bonds were observed at 282, 667, 822, and 991 cm^{-1} in pure MoO_{3-x} and MP photocatalysts. Other peaks in the lower frequency range can be attributed to the phonon vibrations of MoO_{3-x} [36]. The two peaks within range of 1180–1760 cm^{-1} were resulted from the C-C stretching and ring stretching vibrations of PPy. All these results suggested that the successful recombination of PPy and MoO_{3-x}. TG-DSC analysis was exhibited for MoO_{3-x} monomer and MP composite from room temperature to 800 ℃ under N_2 atmosphere to investigate the structure of synthetic photocatalyst. As shown in Fig. S2(a), the exothermic process of MoO_{3-x} can be divided into three parts: the remove of crystalline water, thermal decomposition of metal chelates and complete reduction to MoO_2 [37,38]. Notably, for MP-2, the sustained exothermic process from around 360 ℃ on DSC curve was owing to the thermal decomposition of polypyrrole (Fig. S2(b)) [39].

The morphology and microstructure of pure MoO_{3-x} and MP composite (MP-2) were studied drawing support from SEM, TEM and HRTEM. Fig. S3(a) showed that the fundamental appearance of pure MoO_{3-x} was stacked from nanosheets. With the introduction of PPy, the sheet structure of MoO_{3-x} was disappeared and PPy covered on the surface of MoO_{3-x} leading to the formation of aggregated nanospheres (Fig. S3(b)). From the TEM images of MP-2 (Fig. 2(a-b)), a quasi-core@shell structure can be discovered, corresponding to a dark part of MoO_{3-x} and a transparent part of PPy. HRTEM image of MP-2 was displayed in Fig. 2(c) and pseudo colorization was used to observe the deformation of lattice as the introduction of PPy more intuitively. A significant amount of discontinuous lattice stripe can be obviously observed on MP-2, which may the source for the vacancy generation. As shown in elemental mapping images in Fig. 2(d)-(i), it can be distinctly identified the uniform distribution of Mo, O, C and N elements. To further confirm the quasi-core@shell structure of MP composite, linear region was selected in Fig. 2(e) and the signal strength of each element on it was tested in Fig. 2(j). Notably, the outer transparent area showed more C and N element distribution and less Mo and O element distribution, providing evidence for the existence of PPy shell layer. The successfully construction of conductive polymer layer contributed to the
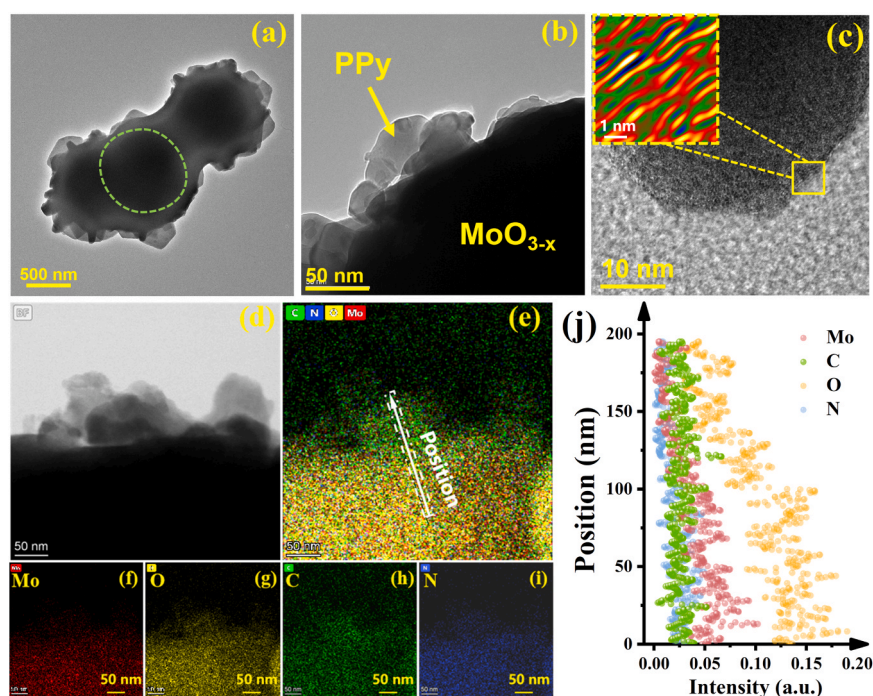

Fig. 2. (a), (b)TEM images of MP-2, (c) HRTEM image of MP-2, (d) - (i) Elemental mapping images of Mo, O, C, N elements in MP-2, (j) The distribution of elements in the selected area.

transmission of free carriers and improvement of photocatalytic desulfurization capability.

The EPR analysis was conducted to investigate unpaired electrons in the photocatalysts. The g-factor is a parameter of molecule motion and its orbital properties [40]. As shown in Fig. 3(a), the g-factor of prepared catalysts was almost constant at 1.929, which was attributed to free electrons. It was obvious that the EPR signal intensity continued to increase as the growth introduction amount of PPy, demonstrating that MP photocatalyst possessed richer free charge carriers and better electron capture ability. Notably, as a type of conductive polymer, polarons and bipolarons will be generated in PPy synthesis, leading to the EPR signal enhancement [41,42]. Therefore, although the free electron density in MP composite continued to increase, it was insufficiency to reflect the difference in oxygen vacancy concentration between different catalysts directly by EPR here. The XPS spectra was determined to further examine the surface electronic states and oxygen vacancy situation. The survey spectra in Fig. S4 revealed that the MP catalysts contained the expected target elements Mo, O, C and N without any other impurities, and the content of different O and Mo forms corresponding to different samples were shown in Fig. S5(a) and Fig. S5(b). In Fig. 3(b), the triple peaks after decomposition at 530.8, 532.2 and 533.7 eV were existed in all of the prepared materials in the O 1s high-resolution spectrum, which were corresponded to the lattice oxygen atoms, oxygen vacancies and hydroxyl oxygen atoms, respectively. Significantly, compared with the pure MoO_{3-x} (11.70%), MP-1 (26.50%) and MP-3 (25.53%), the MP-2 (33.13%) possessed the most oxygen vacancies concentration, which may produced the strongest LSPR effect. The increase quantity of oxygen vacancies with the introduction of PPy may owe to interface bonding effect between MoO_{3-x} and PPy. The addition of PPy promoted the formation of MoO_{3-x} towards amorphous phase and produced lattice distortion leading to higher oxygen vacancy concentration [43]. However, the defect sites may once again be occupied by lone pair electrons on N atoms of pyrrole and caused the fewer oxygen vacancies with the excessive addition of PPy [30]. Fig. 3(c) compared the Mo 3d spectra of the pure MoO_{3-x} and the MP photocatalysts. Peaks at 236.0 and 232.9 eV were pertained to the Mo 3d5/2

and Mo 3d3/2 of Mo^{6+} state, and the peaks at 234.6 and 231.6 eV were belonged to the Mo 3d5/2 and Mo 3d3/2 of Mo^{5+}. A significant increase of the Mo^{5+} amount can be observed with the introduction of PPy which implied that the presence of more surface defects and the higher free electron density, further demonstrating that the formation of more oxygen vacancies [44]. In comparison, the corresponding peaks of Mo 3d of the MP composites presented apparent positive-shift about 0.3 eV, which may be attributed to the generation of high concentration oxygen vacancies. As an electron withdrawing group, oxygen vacancies tended to extract electrons from Mo atoms to balance electron cloud density, ultimately leading to an increasing Mo 3d binding energy [45,46]. Besides, further investigation of valance state of Mo ions was conducted by CV curves in Fig. S6. The reduction peak shifts towards lower angles can be observed. The phenomenon elaborated that the transition of the stronger restoration trend for MP composites from Mo^{6+} to Mo^{5+}. Notably, MP-2 showed stronger current responses compared with MoO_{3-x}, implying the outstanding free electron density and electrochemical reaction rate. As observed in Fig. 3(d), the N 1s of MP composites presented three non-symmetrical peaks located at 397.1, 398.5 and 401.2 eV, corresponding to the Mo-N, -N-H- bonds and $-NH^+$ [47]. The existence of Mo-N bonds provided direct evidence for the strong interfacial interaction between MoO_{3-x} and PPy and the Mo-N bonds could serve as a channel to promote charge transfer. Further detailed spectral analysis of the C elements of MP composites was studied in Fig. S7. The peaks at 286.5 and 284.8 eV in the C1s spectra were resulted from C-N and C-C bonds, respectively, while the peak at 288.7 eV was attributed to the $\pi \rightarrow \pi^*$ transition of PPy. The results manifested the construction of internal conjugated structure of PPy, which was beneficial for electronic transmission [48]. In conclusion, the above results further verified that the successful synthesis of MoO_{3-x}@PPy with rich oxygen vacancy, and a channel for electronic transmission of Mo-N has been constructed.

Based on the above conclusion, the interaction between MoO_{3-x} (MoO_3) and PPy in MP composites with the existence of OV was deeply explored by theoretical calculation to further investigate the mechanism of Mo-N bonds formation. In the first place, the electrostatic potential of
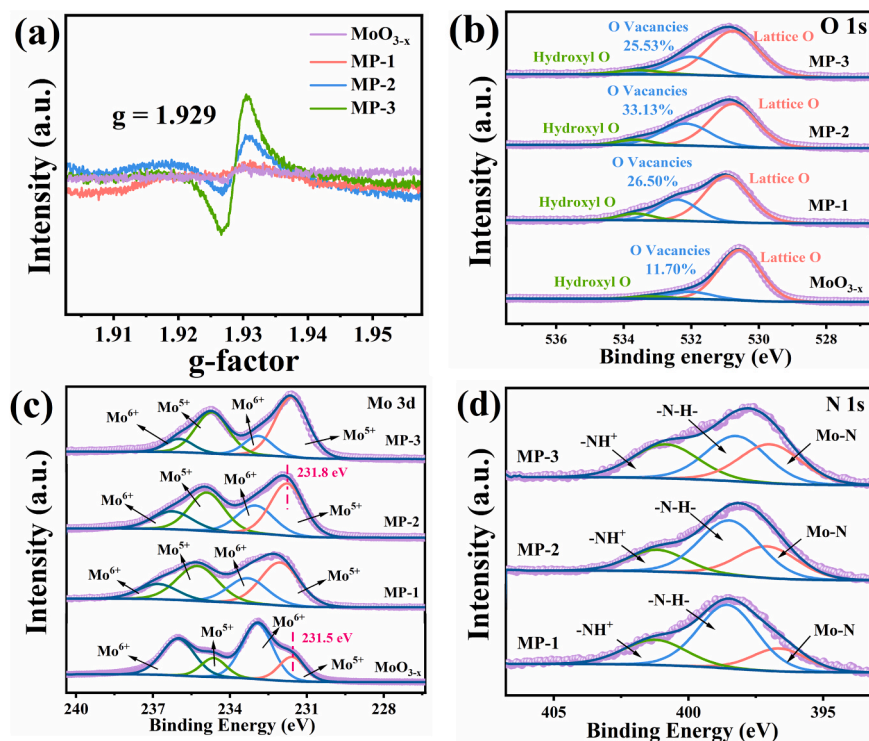

Fig. 3. EPR spectra of the prepared catalysts (a). XPS high-resolution spectra of prepared catalysts: O 1s (b), Mo 3d (c), N 1s (d).

monomers (Fig. 4(a-c)) was plotted to analyze and predict noncovalent interactions [49]. The surfaces of MoO$_3$ (Fig. 4(a)) and MoO$_{3-x}$ (Fig. 4 (b)) plotted in blue indicates positive potential while the surface of PPy (Fig. 4(c)) showing in red means negative potential. Hence, there is a strong electrostatic interaction between MoO$_{3-x}$ (MoO$_3$) and PPy. Besides, the possible configurations of MP composites in the presence or absence of OV were showed in Fig. 4(d) and Fig. 4(e). PPy in MoO$_{3-x}$-PPy (Fig. 4(e)) displays curved, demonstrating the existence of stronger interaction. To reveal chemical bonding and noncovalent interaction regions in MP composites, interaction region indicator (IRI) [50] was performed with the Multiwfn 3.8 (dev) code [51]. As is shown in Fig. 4 (f-g), the dominate interaction in MP composites is the vdW interaction (green region). Note that N-H⋯O hydrogen bonds cannot be neglected in such systems. In contrast, the hydrogen bonding in MoO$_{3-x}$-PPy (Fig. 4 (g)), in view of the blue regions, is much stronger than that in MoO$_3$-PPy (Fig. 4(f)). Between the PPy and MoO$_3$, the interaction energy is −38.0 kcal•mol^{-1} (Table 1). With the introduction of OV, the interaction energy displayed an increase to −44.4 kcal•mol^{-1}, confirming that the existence of OV extremely enhanced the interaction force between PPy and MoO$_{3-x}$. In Table 1, the sign of charge change (Δq) stands for gain (−) or loss (+). Results show that MoO$_3$ gained 0.596 e from PPy whereas MoO$_{3-x}$ gained more charge (1.332 e). In particular, a large number of the obtained charge transferred to Mo atoms of MoO$_{3-x}$-PPy. The results should be attributed to the upgradation of electronic transfer kinetics from heterogeneous interface containing oxygen vacancies and the trend of electron reception by OV, which were more conducive to the born of chemical bonds between MoO$_{3-x}$ and PPy [52,53]. Therefore, the OV is beneficial for interacting between MoO$_{3-x}$ and PPy and plays a significant role in the formation of Mo-N bonds, which provides channels for electron transfer.

3.2. Optical and photoelectric properties

Mott-Schottky (M-S) measurement was conducted to further study the free carrier concentration on the surface of prepared photocatalysts in Fig. 5(a). The negative slope of pure MoO$_{3-x}$ and MP-2 illustrated that the properties of n-type semiconductors. According to the Eq. (3), the

Table 1
Interaction energy (units: kcal•mol^{-1}) and natural population analysis (units: e) of MP composites.

	MoO$_3$-PPy	MoO$_{3-x}$-PPy
E$_{int}$	-38.0	-44.4
Δq(PPy)	+0.596	+1.332
Δq(MoO$_3$, MoO$_{3-x}$)	-0.596	-1.332
Δq(Mo)	-0.055, −0.047, −0.071	-0.223, −0.254, −0.229

free carrier density has negative correlation with the slope of linear portion of M-S curve [54].

$$N_h = (2 \big/ (\varepsilon \varepsilon_0 e_0))[d(2/c^2)dv]^{(-1)} \tag{3}$$

Where N_h represented the hole density, e_0 was the electron charge, ε was the dielectric constant of materials and ε_0 was the vacuum dielectric constant. Therefore, the PPy-composited photocatalyst possessed the higher free carrier density, which may due to the elevation of oxygen vacancy concentration. The rich free density improved the efficiency of transfer of charges and segregation of photocarriers, and enhanced the effect of LSPR. Furthermore, the flat band potential (E_{fb}) of pure MoO$_{3-x}$ and MP composite can be calculated to −0.16 and −0.42 V (vs. Ag/AgCl), which were transformed to 0.04 and −0.22 eV (vs. NHE) by formula of $E_{NHE} = E_{Ag/AgCl} + 0.197$ [55]. In general, conduction band potential (E_{CB}) in n-type semiconductor always roughly 0.2 eV negative than the E_{fb} (vs. NHE). Accordingly, the E$_{CB}$ of MoO$_{3-x}$ and MP composites were extremely estimated as −0.16 and −0.42 eV, respectively [56].

In an effort to further explore the band structure of photocatalyst, VB-XPS was measured to determine valence band of the prepared photocatalysts in Fig. 5(b). The VB potentials of MoO$_{3-x}$ and MP-2 were tested as 2.77 and 2.27 eV, respectively. Therefore, on the basis of reported literature, the potential can be converted into the parallel normal hydrogen electrode (NHE) as 2.53 and 2.03 eV, with the equation of $E_{VB, NHE} = \varphi + E_{VB, XPS}$ - 4.44, where φ is the instrument work function (4.20 eV) [29]. Besides, according to previous studies, the energies of highest occupied molecular orbital (E_{HOMO}) and the lowest unoccupied
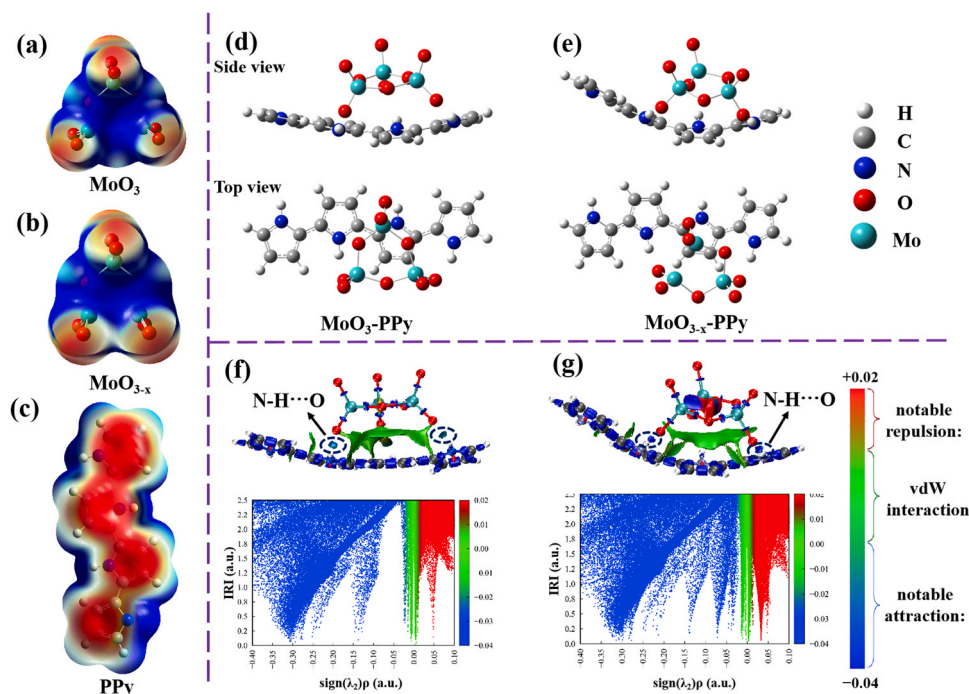

Fig. 4. Electrostatic potential surface mapped on electron total density with an isovalue of 0.001. (a) MoO$_3$, (b) MoO$_{3-x}$, (c) PPy. Optimized configurations of MP composites. (d) MoO$_3$-PPy, (d) MoO$_{3-x}$-PPy. Interaction region indicator (IRI) maps and scatter maps between IRI and sign(λ$_2$)ρ. (f) MoO$_3$-PPy, (g) MoO$_{3-x}$-PPy.
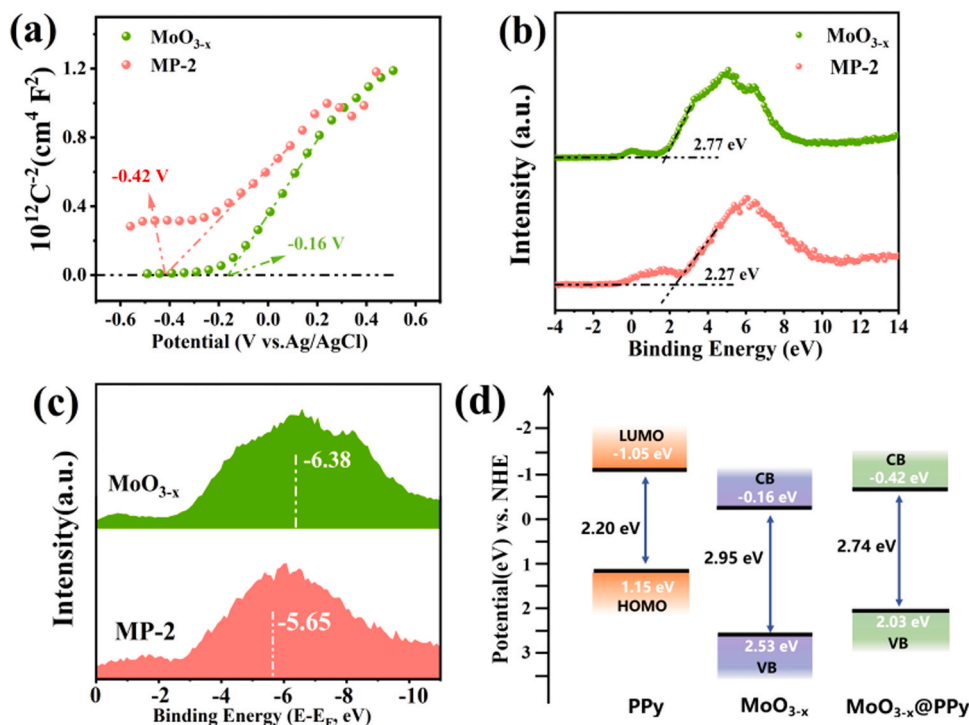
Fig. 5. Mott-Schottky plots of MoO_{3-x} and MP-2 (a). XPS valence band spectra of MoO_{3-x} and MP-2 (b). The *d*-state of MoO_{3-x} and MP-2 (c). Band structure of PPy, MoO_{3-x} and $MoO_{3-x}@PPy$ (d).

molecular orbital (E_{LUMO}) of PPy are generally −1.05 and 1.15 eV, respectively [57,58]. According to the above inference, the CB and VB potential of PPy, pure MoO_{3-x} and MP composite were shown in Fig. 5 (d). The metal *d*-state of pure MoO_{3-x} and MP composite was calculated

by the formula (4) according to the VB-XPS (Fig. 5(c)), which were −6.38 and −5.65 eV, respectively [59]. For transition metals, as the *d*-band center approaches to the Fermi level, the stronger interaction with target sulfur-containing substrate and the more conducive to the
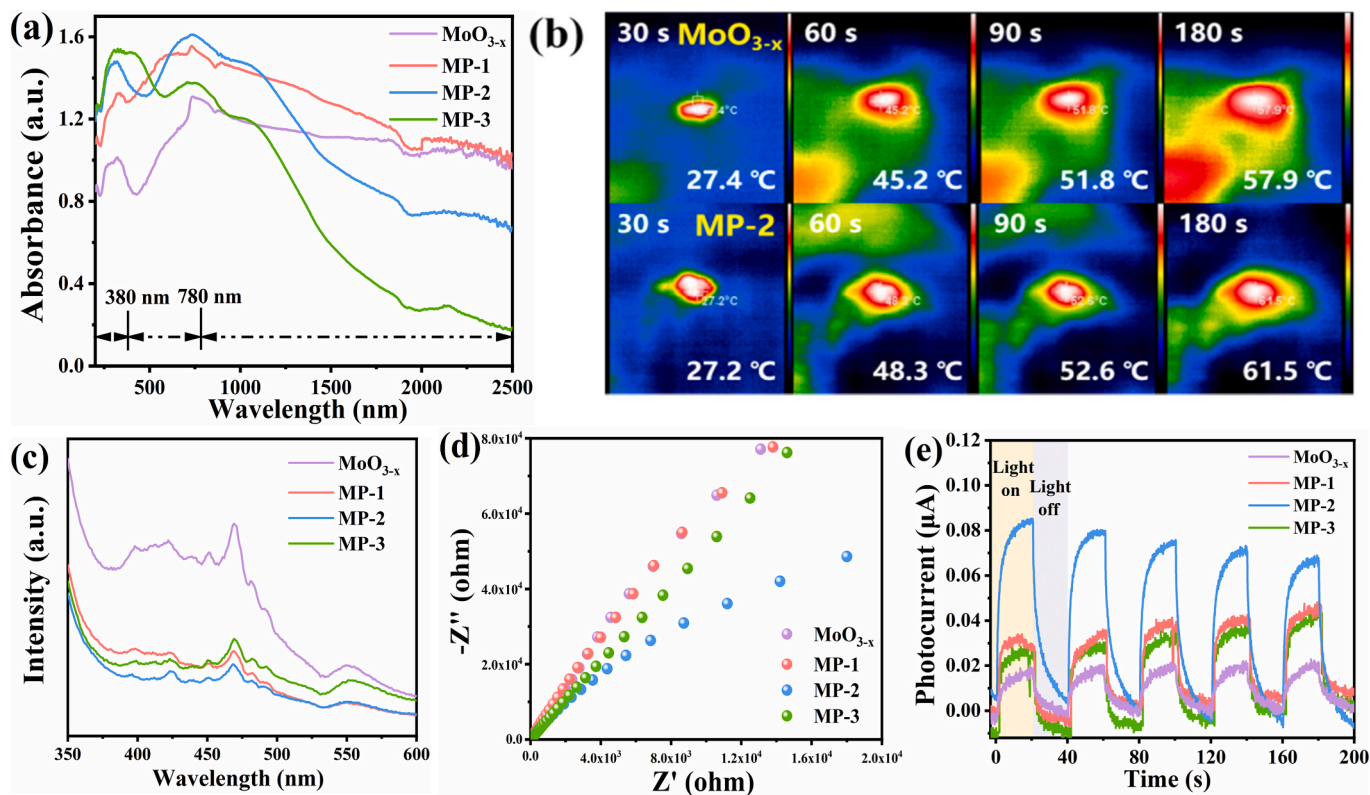

Fig. 6. UV-*Vis*-NIR spectra of prepared samples (a). The IR images of photo-thermal effect for MoO_{3-x} and MP-2 (b). PL spectra (c), EIS spectra (d) and transient photocurrent responses (e) of prepared samples.

desulfurization process can be achieved [60,61]. Obviously, the result indicated that the MP composite possibly presented better catalytic effect on dibenzothiophene sulfide.

$$d = \int N(\varepsilon)\varepsilon d\varepsilon \bigg/ \int N(\varepsilon) \; d\varepsilon \qquad (4)$$

UV-*Vis*-NIR diffuse reflectance spectrum was proceeded to investigate the LSPR effect of prepared photocatalysts. As shown in Fig. 6(a), all of the prepared photocatalysts possessed good absorption in the full spectra and an absorption band around 980 cm^{-1} can be observed, which related to the LSPR effect caused by collective oscillation of surface free carriers [62]. Notably, the MP-2 showed the strongest photoresponse in the range of visible light and near infrared. As observed in Fig. S8, the pure MoO$_{3-x}$ powder exhibited a blue color and MP composite appeared black. It is well known that a dark color typically absorbs light better, which was corresponded to the UV-*Vis*-NIR results [25]. The excellent light absorption performance produced the narrower bandgap, which contributed to the excitation of photogenerated electrons. In order to demonstrate the outstanding light absorption ability brought by LSPR more intuitively, infrared thermal imaging (IR) was tested in Fig. 6(b). The prepared MoO$_{3-x}$ and MP-2 were irradiated under visible light and the real time temperature of the photocatalyst surface was recorded. After 180 s of visible light irradiation, the surface temperature of MoO$_{3-x}$ was raised to 57.9 ℃ and MP-2 could be observed a higher temperature as 61.5 ℃. Obviously, with the higher concentration of surface charge carrier, the MP composite carried the preferable photothermal effect, which owing to the carrier thermalization by phonon modes of the molybdenum oxide under LSPR effect [63]. Photoluminescence (PL), photocurrent responses and electrochemical impedance spectroscopy (EIS) measurements were conducted to investigate the photocatalytic performance of prepared composites. In Fig. 6(c), the PL peak intensity of the catalyst was significantly weakened after composited with PPy and the MP-2 photocatalyst possessed the weakest peak. The result indicated that the increase of oxygen vacancies and the establish of heterojunction boundary composites effectively promoted the migration rate of surface carrier and suppressed recombination of photogenerated e⁻-h⁺. Regarding the EIS test, the Nyquist semicircle radius of composites

showed a significantly reduction after the introduction of PPy (Fig. 6 (d)). The construction of the heterojunction obviously reduced interfacial charge transfer resistance, thereby enhancing the separation of photogenerated charge carriers. The elevated conductive ability may conduce to stronger photocurrent. As known from Fig. 6(e), the MP composites showed the significantly enhanced photocurrent density compared with the pure MoO$_{3-x}$, implying the well charge transfer ability and improved photocatalytic performance. The highest photocurrent peak of MP-2 (0.085 µA), which showed 4.7 times higher than that of pure MoO$_{3-x}$ (0.018 µA), was represented the optimal photo-generated carrier migration ability. In conclusion, the increase of the oxygen vacancy concentration and formation of heterojunction boundary effectively suppressed the photogenerated e⁻-h⁺ pair recombination and enhanced the interface carriers transfer, thereby improving the photocatalytic desulfurization capability.

3.3. Photocatalytic desulfurization performance

In a typical heterogeneous system, the synthetic photocatalysts were introduced coexisting with H$_2$O$_2$ as oxidant to assess the photocatalytic desulfurization capacity. To evaluate the photocatalytic desulfurization capacities of pure MoO$_{3-x}$ and MP composites with various introduction amount of pyrrole, several experiments were conducted with DBT as the target pollutant (Fig. 7(a)). It was found that the photocatalytic desulfurization performance of photocatalyst significantly improved after the compositing with PPy. The pure MoO$_{3-x}$ only reached 44.8% sulfur removal, while, the MP-2 photocatalyst achieved ultra-deep desulfurization with 100% sulfur removal within 60 min. Besides, the desulfurization rate declined to 76.0% with the further introduction of PPy. It can be discovered from Fig. 7(b) that the apparent rate constant (*k*) of above reaction were calculated and MP-2 photocatalyst displayed the fastest reaction rate which owned six times increase compared to pure MoO$_{3-x}$. In particular, the EPODS ability showed a positively correlation with the oxygen vacancy concentration, indicating that the enhanced LSPR effect which owing to the elevating concentration of oxygen vacancy may upgraded the light absorption and visible light utilization of photocatalyst, ultimately improving the photocatalytic desulfurization performance. In addition, different light sources were carried out to
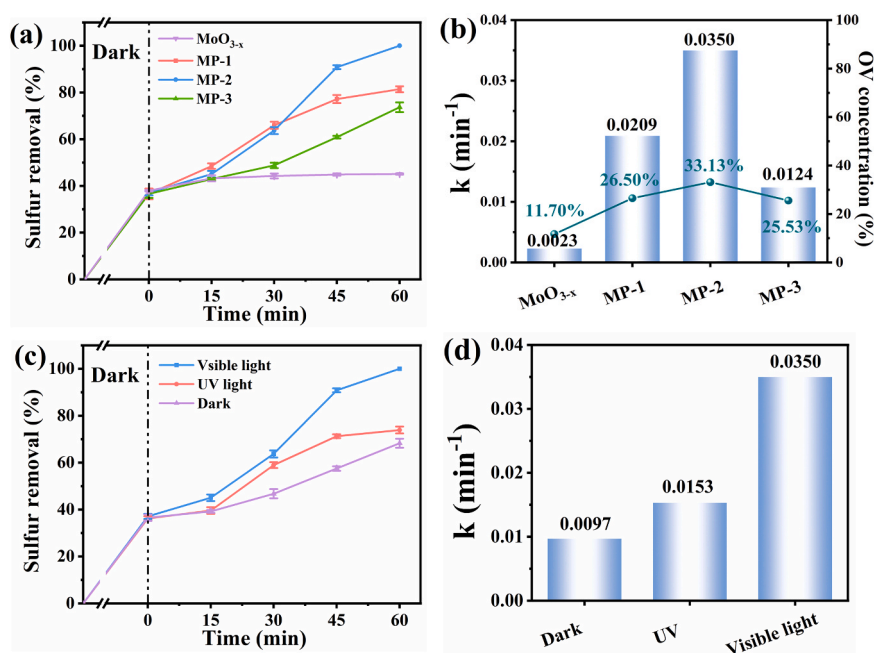

Fig. 7. (a) Photocatalytic sulfur removal rate of all prepared catalysts. (b) The OV concentration and apparent rate constant of different samples in desulfurization reaction. (c) Photocatalytic desulfurization of MP-2 with different light sources. (d) Apparent rate constant of reaction under different light sources. Reaction conditions: Visible light, room temperature (298 K), 0.03 g catalyst, O/S = 3:1, 5 mL of MeCN and 10 mL of model oil.

illustrated the impression of LSPR effect to photocatalytic desulfurization result. The sulfur removal rate can reach 100.0% in 60 min under visible light and only 74.3% desulfurization rate can be achieved under UV irradiation (Fig. 7(c)), attributing to the well photo-response in the range of visible light under the LSPR effect. The phenomena also consistent with the results of UV-*Vis*-NIR diffuse reflectance spectrum. Furthermore, the Fig. 7(d) displayed that the *k* of visible light is 0.035 min^{-1}, almost 2.3 and 3.5 times that of reaction under UV light and dark, respectively. The above results indicated that the desulfurization ability of LSPR-enhanced photocatalyst shows a significant improvement under visible light.

Exploration was conducted on the performance of various reaction elements of EPODS to determine the necessary conditions in the system. As shown in Fig. 8(a), it can be discovered that the desulfurization rate was only 9.0% without MeCN and 37% without H$_2$O$_2$, respectively. Furthermore, the sulfur removal rate reached 70.2% without visible light. Therefore, only with the introduction of photocatalyst, oxidant, extractant and visible light, the deep desulfurization can be achieved. Further exploration of the optimal reaction conditions for the EPODS system was carried out. The effect of hydrogen peroxide dosage on the desulfurization ability of the photocatalyst was explored by regulating the molar ratio of H$_2$O$_2$ to DBT (O/S) in Fig. 8(b). Only 82.8% EPODS rate can be obtained when the O/S ratio raised to 2, and the sulfur removal rate increased to 100% as the O/S ratio rose to 3. The sufficient H$_2$O$_2$ generated enough reactive oxygen species, which promoting the progress of the photocatalytic desulfurization reaction. It can be also observed that the desulfurization rate was declined with the 4:1 O/S ratio of H$_2$O$_2$, which may due to the excessive hydrogen peroxide producing too much water and inhibiting the mass transfer [64]. The effect of catalyst dosage to desulfurization performance was demonstrated in Fig. 8(c). The EPODS rate reached 88.2% as 0.02 g MP-2 using, while a 100.0% sulfur removal rate can be realized with 0.03 g photocatalyst. When few amounts of catalyst were used, the limited number of active sites obstructed to deep desulfurization. However, the EPODS rate decreased to 85.6% with the further introduction of MP-2, which may attribute to that excessive amount of catalyst hindered the transmittance

of visible light. In addition, to investigate the EPODS ability in high sulfur concentrations, photocatalytic desulfurization performance of photocatalyst was also tested with three concentrations of model oil (Fig. S9). The ultra deep desulfurization all can be achieved in 60 min, with initial DBT content of 200, 400 and 600 ppm in the model oil. Then, the photocatalytic desulfurization performance of the photocatalyst for other dibenzothiophene sulfides was considered and the desulfurization capacity on DBT, 4-MDBT and 4,6-DMDBT were tested in Fig. 8(d). The EPODS activities of three different substrates were compared within 2 h, following the order of DBT (100.0%) > 4-MDBT (87.4%) > 4,6-DMDBT (84.9%). The diversity of different thiophene sulfides removal performance may owing to the steric hindrance originating from methyl [65]. The additional methyl group on the benzene ring of 4-MDBT and 4,6-DMDBT highly weaking the availability of active sites to S atoms which leads to the lower reaction rate and efficiency. Based on the above results, the LSPR-enhanced photocatalyst prepared in this study demonstrated superior photocatalytic desulfurization performance when compared to other recently published desulfurization photocatalysts listed in Table S1 [11,66–69].

3.4. Selectivity and recycling of photocatalyst

In real oil, apart from dibenzothiophene sulfur compounds, many other aliphatic hydrocarbons and aromatic compounds also exist and possible occur competitive reaction during the desulfurization process, affecting the efficiency of sulfur removal. Therefore, it is necessary to examine the selectivity of catalyst for DBT when these compounds coexist. Cyclohexene, p-xylene and cyclohexane were introduced to the EPODS system as interfering substances to simulate the effects of olefins and aromatics on the reaction system, respectively. It can be observed in Fig. 9(a) that the addition of p-xylene, cyclohexene and cyclohexane had seldom inhibitory effects on the removal of DBT. Besides, by extending the reaction time, a deep desulfurization efficiency of 100%, 96.6% and 95.7% can be obtained, respectively. The results demonstrated that the MP photocatalyst exhibited well resistance to interference and selectivity, which provided guarantee for the practical application.
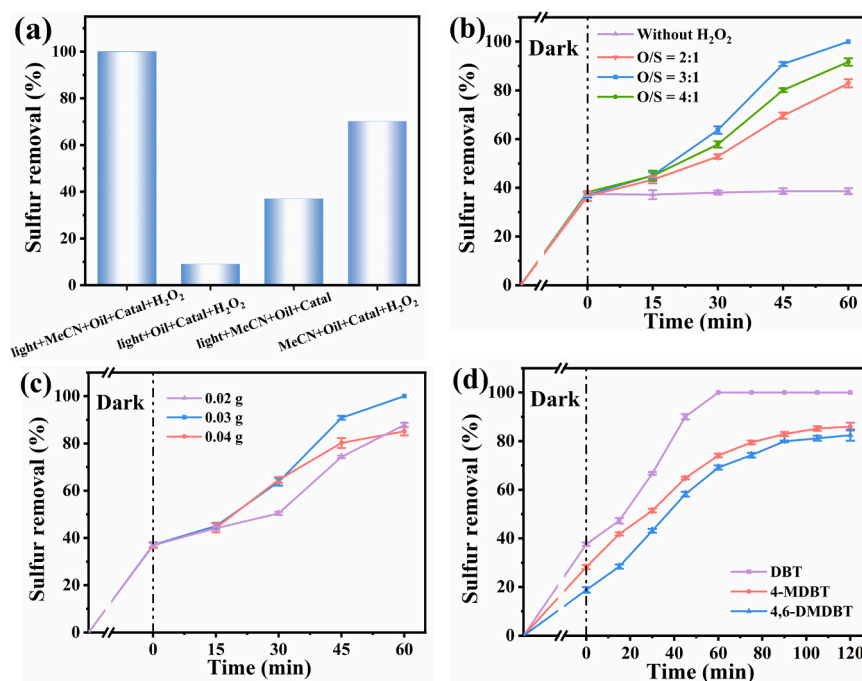

Fig. 8. Photocatalytic desulfurization performance of prepared catalysts with different photocatalytic reaction systems (a). Effect of different H$_2$O$_2$/sulfur molar ratio (b) and catalyst dosage (c) on photocatalytic of MP-2. The photocatalytic activity of different sulfur containing substrates (d). Reaction conditions: Visible light, room temperature (298 K), 0.03 g catalyst, O/S = 3:1, 5 mL of MeCN and 10 mL of model oil.).
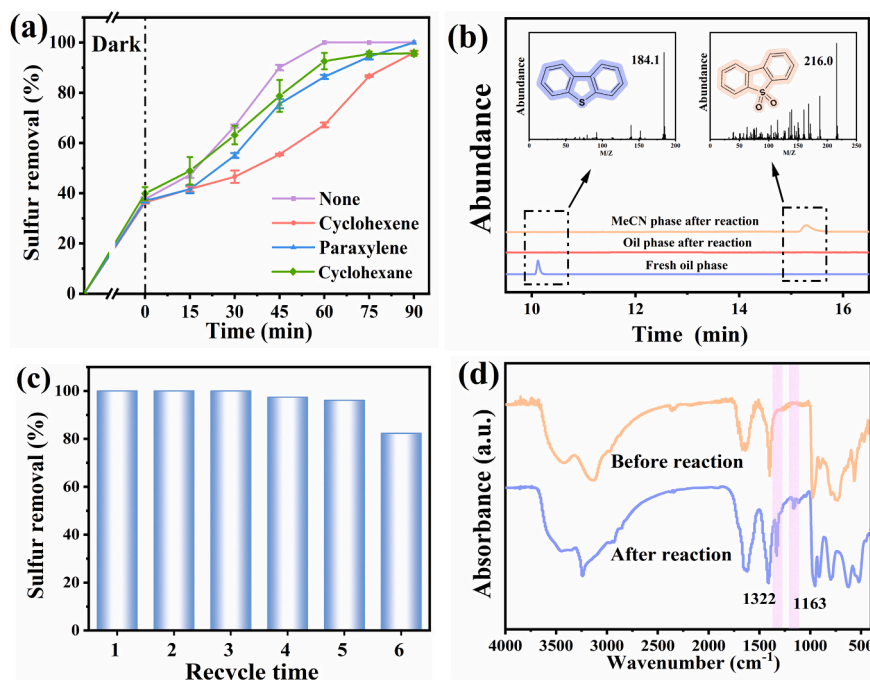
Fig. 9. (a) The impact of aromatic, olefin and alicyclic hydrocarbon interferences on the efficiency of desulfurization. (b) GC-MS analysis of the EPODS system. (c) The recycle performance of MP-2. (d) FT-IR spectra of fresh MP-2 and used MP-2 photocatalyst.

To deep inform the final product in EPODS process, GC-MS analysis was implemented to analyze the products after the reaction in Fig. 9(b). The peak of DBT ($M/Z = 184.1$) was disappeared after the reaction and the peak of $DBTO_2$ ($M/Z = 216.0$) was apparently observed in MeCN-catalyst phase, illustrating that the DBT was fully converted to $DBTO_2$ and it was reserved in extractant phase due to the strong polarity. Furthermore, the characteristic peak of DBT was failed to be detected after the reaction, demonstrating that the successfully removal of the sulfur-containing substrate from the model oil and achieved the purpose of clean oil. As displayed in Fig. 9(c), the cyclability of MP photocatalyst was investigated. The reused photocatalyst was recovered by stoving at 60 ºC for 12 h to remove water and acetonitrile for next utilization with equal conditions. The EPODS rate was remained 96.1% after the completion of the fifth cycle, which achieved the ultra-deep desulfurization standard. The results suggested that the photocatalyst exhibited excellent cycling stability. The decline in EPODS performance to 82.3% in the sixth cycle may be resulted from the coverage of the active sites by the reaction product sulfone. Then, FT-IR spectra of fresh and recycled MP photocatalyst were compared in Fig. 9(d) to further interpret the reason for the decline in desulfurization performance. It can be observed that the basic structure of MP was reserved, confirming that the outstanding steadily performance of MP photocatalyst. Notably, several new characteristic peaks can be seen on used photocatalyst, and peaks at

1163 and 1322 cm^{-1} can be considered as the S=O on the $DBTO_2$ [70]. The phenomenon further proved the impact of sulfone products after the reaction on the catalytic cycling performance.

3.5. Proposed photocatalytic mechanism of MP system

To explore whether the radical that played a primary role during the photocatalytic desulfurization reaction, radical quenching tests were applied and reflected in Fig. 10(a). Classically, BQ was selected as a $\bullet O_2^-$ scavenger, h^+ was inhibited with TEOA and the effect of $\bullet OH$ can be suppressed by DMSO [71,72]. The EPODS efficiency was slightly suppressed as the introduction of BQ. Nevertheless, a significantly weakened of desulfurization performance can be observed under the impression of DMSO and $NaHCO_3$. Therefore, it can be deduced that $\bullet OH$ and h^+ work as probable active radical [73,74]. To further prove above hypothesis, ESR analysis was carried out with DMPO and TEMPO as the function of trapping agent for $\bullet OH$ and h^+, respectively. It was noteworthy that no signal peak can be surveyed before the introduction of oxidant and visible light, and obvious quadruple signal peak can be observed which was pertained to DMPO-$\bullet OH$ after 20 min of reaction with H_2O_2 and visible light (Fig. 10(b)) [75]. Furthermore, the characteristic signal of TEMPO-h^+ was significantly reduced after 20 min reaction, implying the generation of photogenerated hole (Fig. 10(c))
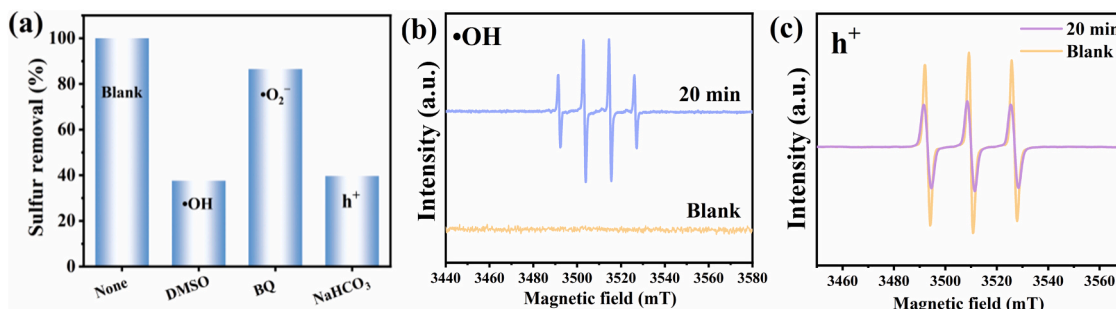

Fig. 10. Free radical quenching test (a). ESR spectra of $\bullet OH$ (b) and h^+ (c) active radicals on the MP-2.

[76]. The above phenomenon was well corresponded to the conclusion of free radical quenching experiment and further confirmed that •OH and h^+ were taken for the primary reactive radicals in EPODS system.

According to the above results, a potential photocatalytic desulfurization mechanism in the EPDOS system was proposed in Scheme 2. Firstly, a portion of DBT was extracted from oil phase to MeCN phase during stirring efficiency of dark reaction due to the diversity in polarity between oil and MeCN. After that, the introducing H_2O_2 as an oxidant was adsorbed to the surface of MP photocatalyst. Under the irradiation of visible light, with the enhanced concentration of oxygen vacancies on the surface of MP, abundant free charges displayed intensive oscillation which was aligned with the phase of the fluctuation in the electric field of incoming light [77]. Then the energy of photons was greatly absorbed and brought outstanding photoresponse ability. To illustrate the above process more intuitively, the IR image of MP photocatalyst in MeCN was further investigated (Fig. S10). After 10 min of light irradiation, the surface temperature of MeCN-catalyst solution was raised to 31.5 °C, which showed the significantly promoted photothermal effect contrasting with the blank MeCN sample (24.8 °C). The specific temperature variation with irradiation time was shown in Fig. S11. Therefore, the outstanding light absorption ability ensured the well photocatalytic desulfurization performance of MP. Furthermore, owing to the discrepancy of band structure between MoO_{3-x} and PPy, the *E*-filed was formed and driven stimulated e^- directional migrated from the CB of MoO_{3-x} to HOMO of PPy. In this procedure, the chemical bonding interface Mo-N bonds serve as the channel for rapid electron transfer, which facilitating effective separation of e^--h^+ pairs. Afterwards, e^- were accumulated on the LUMO of PPy and high electron concentration locally demonstrated enhanced reduction capability, effectively activating H_2O_2 to generate •OH and OH^- reactive species (Eq. (6)). Then OH^- was able to react with h^+ on the VB of MoO_{3-x} and promoted the further generation of •OH (Eq. (7)). Significantly, due to the fact that h^+ was inclined to accept electron, it directly contributed to the oxidation reaction of electron-rich S atom on DBT as oxidant. Ultimately, DBT was oxidized to $DBTO_2$ under the combined action of •OH and h^+ (Eq. (8)). The conversion of radicals as follow:

$$MoO_{3-x}@PPy + hv \rightarrow e^- + h^+ \tag{5}$$

$$e^- + H_2O_2 \rightarrow \bullet OH + OH^- \tag{6}$$

$$h^+ + OH^- \rightarrow \bullet OH \tag{7}$$

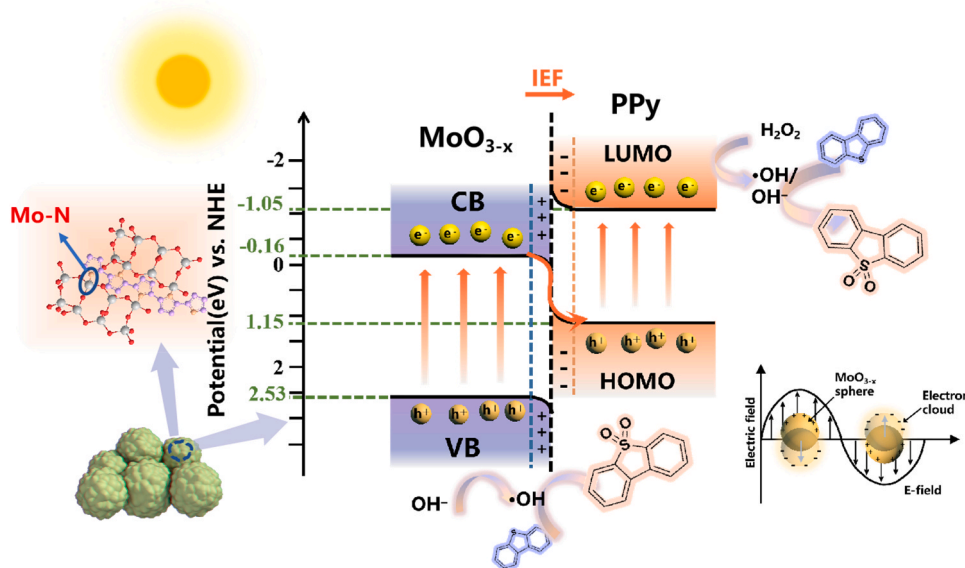$$\bullet OH / h^+ + DBT \rightarrow DBTO_2 \tag{8}$$

4. Conclusion

In general, several LSPR effect enhanced S-scheme heterojunction $MoO_{3-x}@PPy$ photocatalysts with a chemical interfacial Mo-N bond are designed. The introduction of polypyrrole conduces to formation of rich oxygen vacancies, which exhibits a wide range of light absorption. The built-in electron field accelerates the diversion of photo-generated charges and drives the separation of photocarriers. The synergistic effect of the aforementioned factors enhances the photocatalytic desulfurization performance of $MoO_{3-x}@PPy$. Subsequently, ultra deep desulfurization can be achieved in 60 min and well stability is persisted within five cycles. The relevant analysis proved that •OH and h^+ are major free radicals and $DBTO_2$ is the main product in EPODS system, and a potential electron transfer mechanism of S-scheme heterojunction is put forward. In brief, this work provides a catalyst possessing broad spectrum light absorption capacity with green and efficient energy conversion, extending a completely new understanding of the impact of LSPR effect and heterojunction interface charge transfer on the photocatalytic desulfurization ability.

CRediT authorship contribution statement

Huaming Li: Supervision, Resources. **Wenshuai Zhu:** Resources, Methodology. **Jie Yin:** Writing – review & editing, Visualization, Software. **Suhang Xun:** Writing – review & editing, Supervision, Formal analysis, Conceptualization. **Chenchao Hu:** Writing – review & editing, Writing – original draft, Investigation, Data curation. **Minqiang He:** Project administration, Funding acquisition. **Peiwen Wu:** Supervision, Conceptualization. **Linhua Zhu:** Project administration, Funding acquisition. **Hongping Li:** Supervision, Methodology, Conceptualization.

Declaration of Competing Interest

The authors declare that they have no known competing financial interests or personal relationships that could have appeared to influence the work reported in this paper.

Scheme 2. Prospective reaction mechanisms of EPODS over MP.

Appendix A. Supporting information

Supplementary data associated with this article can be found in the online version at doi:10.1016/j.apcatb.2024.124155.

References

[1] W. Jiang, X. An, J. Xiao, et al., Enhanced oxygen activation achieved by robust single chromium atom-derived catalysts in aerobic oxidative desulfurization, ACS Catal. 12 (2022) 8623–8631.

[2] M. Ahmad, M. Yousaf, W. Cai, et al., Formulation of heterometallic ZIF-8@Cu/Ni/ZnO@CNTs heterostructure photocatalyst for Ultra-Deep desulphurization of coal and fuels, Chem. Eng. J. 453 (2023) 139846.

[3] P. Wu, X. Song, L. Chen, et al., Few-layered hexagonal boron nitride nanosheets stabilized Pt NPs for oxidation promoted adsorptive desulfurization of fuel oil, Green. Energy Environ. (2022), https://doi.org/10.1016/j.gee.2022.08.003.

[4] J. Liu, X. Liu, R. Yan, et al., Active phase morphology engineering of NiMo/Al$_2$O$_3$ through La introduction for boosting hydrodesulfurization of 4,6-DMDBT, Pet. Sci. 20 (2023) 1231–1237.

[5] J. Zou, Y. Lin, S. Wu, et al., Molybdenum dioxide nanoparticles anchored on nitrogen-doped carbon nanotubes as oxidative desulfurization catalysts: role of electron transfer in activity and reusability, Adv. Funct. Mater. 31 (2021) 2100442.

[6] Q. Cheng, Y. He, V. Pavlinek, et al., Surfactant-assisted polypyrrole/titanate composite nanofibers: Morphology, structure and electrical properties, Synth. Met. 158 (2008) 953–957.

[7] J. Zhu, J. Yu, P. Wu, et al., 3D printing of the multifunctional fixed-bed reactor and matched 3D-CeO$_2$ / ATP monolithic adsorbent for adsorption desulfurization, Chem. Eng. J. 468 (2023) 143590.

[8] S. Balendhran, S. Walia, H. Nili, et al., Two-dimensional molybdenum trioxide and dichalcogenides, Adv. Funct. Mater. 23 (2013) 3952–3970.

[9] P. Wu, C. Deng, P. Liu, et al., An ultra-stable high entropy metal nitride for aerobic oxidative desulfurization and source recovery of aromatic sulfides from fuel oils, Chem. Eng. J. 474 (2023) 145850.

[10] J. Liu, L. Zhang, J. Zhu, et al., Size-dependent surface electronic structure of V$_2$O$_5$/TiO$_2$ for ultra-deep aerobic oxidative desulfurization of diesel, Chem. Eng. Sci. 275 (2023) 118749.

[11] X. Zhou, T. Wang, L. Zhang, et al., Highly efficient Ag$_2$O/Na-g-C$_3$N$_4$ heterojunction for photocatalytic desulfurization of thiophene in fuel under ambient air conditions, Appl. Catal., B 316 (2022) 121614.

[12] L. Chen, J. Ren, H. Wang, et al., Engineering a local hydrophilic environment in fuel oil for efficient oxidative desulfurization with minimum H$_2$O$_2$ oxidant, ACS Catal. 13 (2023) 12125–12133.

[13] D. Zhu, K. Zhu, L. Xu, et al., Co-based metal-organic frameworks confined N-hydroxyphthalimide for enhancing aerobic desulfurization of diesel fuels, Fuel 356 (2024) 129599.

[14] D. Liu, C. Xue, Plasmonic coupling architectures for enhanced photocatalysis, Adv. Mater. 33 (2021) 2005738.

[15] X. Wu, W. Zhang, J. Li, et al., Identification of the active sites on metallic MoO$_{2-x}$ nano-sea-urchin for atmospheric CO$_2$ photoreduction under UV, vsible, and near-infrared light illumination, Angew. Chem. Int. Ed. Engl. 62 (2022) e202213124.

[16] K. Ren, P. Yin, Y. Zhou, et al., Localized defects on copper sulfide surface for enhanced plasmon resonance and water splitting, Small 13 (2017) 1700867.

[17] X. Ma, Y. Dai, L. Yu, et al., Energy transfer in plasmonic photocatalytic composites, Light-Sci. Appl. 5 (2016) e16017.

[18] W. Huang, H. Meng, Y. Gao, et al., Metallic tungsten carbide nanoparticles as a near-infrared-driven photocatalyst, J. Mater. Chem. A 7 (2019) 18538–18546.

[19] X. Zhang, Y.L. Chen, R. Liu, et al., Plasmonic photocatalysis, Rep. Prog. Phys. 76 (2013) 046401.

[20] M. Sayed, J. Yu, G. Liu, et al., Non-noble plasmonic metal-based photocatalysts, Chem. Rev. 122 (2022) 10484–10537.

[21] Z. Ahmadzadeh, M. Ranjbar, Plasmonic MoO$_{3-x}$ nanosheets by anodic oxidation of molybdenum for colorimetric sensing of hydrogen peroxide, Anal. Chim. Acta 1198 (2022) 339529.

[22] Y. Yang, C. Niu, D. Huang, et al., Appropriate oxygen vacancies and Mo-N bond synergistically modulate charge transfer dynamics of MoO$_{3-x}$/S-CN for superior photocatalytic disinfection: Unveiling synergistic effects and disinfection mechanism, J. Hazard. Mater. 445 (2023) 130481.

[23] J. Wang, Y. Yang, H. Li, et al., Stable and tunable plasmon resonance of molybdenum oxide nanosheets from the ultraviolet to the near-infrared region for ultrasensitive surface-enhanced Raman analysis, Chem. Sci. 10 (2019) 6330–6335.

[24] Z. Zhang, B. Xi, X. Wang, et al., Oxygen defects engineering of VO$_2$ center dot xH$_{(2)}$O nanosheets via in situ polypyrrole polymerization for efficient aqueous zinc ion storage, Adv. Funct. Mater. 31 (2021) 2103070.

[25] J. Li, Y. Ye, L. Ye, et al., Sunlight induced photo-thermal synergistic catalytic CO$_2$ conversion via localized surface plasmon resonance of MoO$_{3-x}$, J. Mater. Chem. A 7 (2019) 2821–2830.

[26] M.J. Frisch, G.W. Trucks, H.B. Schlegel, et al., Gaussian 16 Rev. B.01, (2016).

[27] P.J. Stephens, F.J. Devlin, C.F. Chabalowski, et al., Ab initio calculation of vibrational absorption and circular dichroism spectra using density functional force fields, J. Phys. Chem. 98 (1994) 11623–11627.

[28] J. Wang, H. Liu, R. Zhou, et al., Onion-like nanospheres organized by carbon encapsulated few-layer MoS$_2$ nanosheets with enhanced lithium storage performance, J. Power Sources 413 (2019) 327–333.

[29] X. Li, B. Kang, F. Dong, et al., Enhanced photocatalytic degradation and H$_2$/H$_2$O$_2$ production performance of S-pCN/WO$_{2.72}$ S-scheme heterojunction with appropriate surface oxygen vacancies, Nano Energy 81 (2021) 105671.

[30] C. Cheng, S. Zong, J. Shi, et al., Facile preparation of nanosized MoP as cocatalyst coupled with g-C$_3$N$_4$ by surface bonding state for enhanced photocatalytic hydrogen production, Appl. Catal., B 265 (2020) 118620.

[31] J. Zheng, J. Chen, M. Zhu, et al., Synergetic enhancement of electrical conductivity and infrared emissivity of SiC-MoSi$_2$ ceramics via N doping, J. Eur. Ceram. Soc. 42 (2022) 3738–3746.

[32] Y. Wang, Z. Zhong, Y. Muhammad, et al., Defect engineering of NH$_2$-MIL-88B(Fe) using different monodentate ligands for enhancement of photo-Fenton catalytic performance of acetamiprid degradation, Chem. Eng. J. 398 (2020) 125684.

[33] A. Rajendran, H. Fan, T. Cui, et al., Octamolybdates containing Mo^V and Mo^{VI} sites supported on mesoporous tin oxide for oxidative desulfurization of liquid fuels, J. Clean. Prod. 334 (2022) 130199.

[34] Y. Ren, D. Feng, Z. Yan, et al., Interfacial coupled engineering of plasmonic amorphous MoO$_{3-x}$ nanodots/g-C$_3$N$_4$ nanosheets for photocatalytic water splitting and photothermal conversion, Chem. Eng. J. 453 (2023) 139875.

[35] Y. Han, T. Wang, T. Li, et al., Preparation and electrochemical performances of graphene/polypyrrole nanocomposite with anthraquinone-graphene oxide as active oxidant, Carbon 119 (2017) 111–118.

[36] M. Dieterle, G. Weinberg, G. Mestl, Raman spectroscopy of molybdenum oxides - Part I. Structural characterization of oxygen defects in MoO$_{3-x}$ by DR UV/VIS, Raman spectroscopy and X-ray diffraction, Phys. Chem. Chem. Phys. 4 (2002) 812–821.

[37] L. Wuji, Z. Qiaoying, C. Lifang, et al., Preparation of oxygen defect vacancies MoO$_{3-x}$ and its adsorption properties, CIESC J. 70 (2019) 3956–3966.

[38] C. Li, H. Jang, M.G. Kim, et al., Ru-incorporated oxygen-vacancy-enriched MoO$_2$ electrocatalysts for hydrogen evolution reaction, Appl. Catal., B 307 (2022) 121204.

[39] J. Ding, L. Wang, Y. Zhao, et al., Boosted interfacial polarization from multishell TiO$_2$@Fe$_3$O$_4$@PPy heterojunction for enhanced microwave absorption, Small 15 (2019) 1902885.

[40] Z. Wang, W. Ma, C. Chen, et al., Probing paramagnetic species in titania-based heterogeneous photocatalysis by electron spin resonance (ESR) spectroscopy-a mini review, Chem. Eng. J. 170 (2011) 353–362.

[41] T.R. Naveen Kumar, P. Karthik, B. Neppolian, Polaron and bipolaron induced charge carrier transportation for enhanced photocatalytic H$_2$ production, Nanoscale 12 (2020) 14213–14221.

[42] B.H. Kim, S. Kim, S. Kim, et al., Charge dynamics on size confined conducting polymers through electron paramagnetic resonance spectroscopy, Org. Electron. 85 (2020) 105807.

[43] S. Yang, Z. Qi, Y. Wen, et al., Generation of abundant oxygen vacancies in Fe doped δ-MnO$_2$ by a facile interfacial synthesis strategy for highly efficient catalysis of VOCs oxidation, Chem. Eng. J. 452 (2023) 139657.

[44] J. Xiong, J. Di, J. Xia, et al., Surface defect engineering in 2D nanomaterials for photocatalysis, Adv. Funct. Mater. 28 (2018) 1801983.

[45] L. Zhang, J. Zhang, H. Yu, et al., Emerging S-Scheme photocatalyst, Adv. Mater. 34 (2022) 2107668.

[46] X. Wang, X. Wang, J. Huang, et al., Interfacial chemical bond and internal electric field modulated Z-scheme S-v-ZnIn$_2$S$_4$/MoSe$_2$ photocatalyst for efficient hydrogen evolution, Nat. Commun. 12 (2021) 4112.

[47] A. Xie, X. Lin, C. Zhang, et al., Oxygen vacancy mediated polymerization of pyrrole on MoO$_3$ to construct dielectric nanocomposites for electromagnetic waves absorption application, J. Alloy. Compd. 938 (2023) 168523.

[48] Y. Li, S. Yan, X. Jia, et al., Uncovering the origin of full-spectrum visible-light-responsive polypyrrole supramolecular photocatalysts, Appl. Catal., B 287 (2021) 119926.

[49] J. Yin, J. Zhang, C. Wang, et al., Theoretical insights into CO$_2$/N$_2$ selectivity of the porous ionic liquids constructed by ion-dipole interactions, J. Mol. Liq. 344 (2021) 117676.

[50] T. Lu, Q. Chen, Interaction region indicator: A simple real space function clearly revealing both chemical bonds and weak interactions, Chem. -Methods 1 (2021) 231–239.

[51] T. Lu, F. Chen, Multiwfn: a multifunctional wavefunction analyzer, J. Comput. Chem. 33 (2012) 580–592.

[52] N. Wu, P. Chien, Y. Qian, et al., Enhanced surface interactions enable fast Li^+ conduction in oxide/polymer composite electrolyte, Angew. Chem. Int. Ed. Engl. 59 (2020) 4131–4137.

[53] R. Shen, G. Liang, L. Hao, et al., In situ synthesis of chemically bonded 2D/2D covalent organic frameworks/O-vacancy WO_3 Z-Scheme heterostructure for photocatalytic overall water splitting, Adv. Mater. 35 (2023) 2303649.

[54] M. Wang, G. Tan, D. Zhang, et al., Defect-mediated Z-scheme $BiO_{2-x}/Bi_2O_{2.75}$ photocatalyst for full spectrum solar-driven organic dyes degradation, Appl. Catal., B 254 (2019) 98–112.

[55] C. Hu, S. Xun, D. Liu, et al., Construction of 3D mesoporous silica supported MoO_3 nanoparticles for the efficient photocatalytic oxidative desulfurization under visible light, Sep. Purif. Technol. 334 (2024) 126032.

[56] L. Fan, S. Lei, S.M.K. Sari, et al., Controllable S-Vacancies of monolayered Mo-S nanocrystals for highly harvesting lithium storage, Nano Energy 78 (2020) 105235.

[57] T. Li, K. Wang, Q.-T. Fang, et al., Conductive polymer supported and confined iron phosphide nanocrystals for boosting the photocatalytic hydrogen production of graphitic carbon nitride, J. Mater. Chem. C 8 (2020) 14540–14547.

[58] Y. Yang, S. Ma, J. Qu, et al., Transforming type-II Fe_2O_3@polypyrrole to Z-scheme Fe_2O_3@polypyrrole/Prussian blue via Prussian blue as bridge: Enhanced activity in photo-Fenton reaction and mechanism insight, J. Hazard. Mater. 405 (2021) 124668.

[59] S.J. Hwang, S.K. Kim, J.G. Lee, et al., Role of Electronic Perturbation in Stability and Activity of Pt-Based Alloy Nanocatalysts for Oxygen Reduction, J. Am. Chem. Soc. 134 (2012) 19508–19511.

[60] J.K. Norskov, T. Bligaard, J. Rossmeisl, et al., Towards the computational design of solid catalysts, Nat. Chem. 1 (2009) 37–46.

[61] J. Xiong, J. Li, H. Huang, et al., Electronic state tuning over Mo-doped $W_{18}O_{49}$ ultrathin nanowires with enhanced molecular oxygen activation for desulfurization, Sep. Purif. Technol. 294 (2022) 121167.

[62] Z. Tao, J. Feng, F. Yang, et al., Plasmon-enhanced photocatalysis using gold nanoparticles encapsulated in nanoscale molybdenum oxide shell, Nanotechnology 34 (2023) 155604.

[63] R.C. Elias, S. Linic, Elucidating the roles of local and nonlocal rate enhancement mechanisms in plasmonic catalysis, J. Am. Chem. Soc. 144 (2022) 19990–19998.

[64] X. Xing, H. Guo, T. He, et al., Tungstovanadate-based ionic liquid catalyst $[C_2(MIM)_2]_2VW_{12}O_{40}$ used in deep desulfurization for ultraclean fuel with simultaneous recovery of the sulfone product, ACS Sustain. Chem. Eng. 10 (2022) 11533–11543.

[65] H. Li, W. Zhu, S. Zhu, et al., The selectivity for sulfur removal from oils: An insight from conceptual density functional theory, AIChE J. 62 (2016) 2087–2100.

[66] X. Li, W. Zhu, X. Lu, et al., Integrated nanostructures of CeO_2/attapulgite/g-C_3N_4 as efficient catalyst for photocatalytic desulfurization: Mechanism, kinetics and influencing factors, Chem. Eng. J. 326 (2017) 87–98.

[67] M. Abdollahi, A. Larimi, Z. Jiang, et al., Photocatalytic oxidative desulfurization of model fuel over visible light-active Cu-impregnated carbon-doped TiO_2, J. Clean. Prod. 380 (2022) 134968.

[68] X. Lu, W. Chen, H. Hou, et al., Preparation of two-dimensional layered CeO_2/Bi_2O_3 composites for efficient photocatalytic desulfurization, Catalysts 13 (2023) 821.

[69] A.A. Ismail, S.M. Albukhari, L.A. Al-Hajji, Fabrication of $BiVO_4$ nanosheets decorating by V_2O_5 nanoparticles for the enhanced photocatalytic desulfurization of thiophene, J. Environ. Chem. Eng. 11 (2023) 109429.

[70] S. Xun, W. Jiang, T. Guo, et al., Magnetic mesoporous nanospheres supported phosphomolybdate-based ionic liquid for aerobic oxidative desulfurization of fuel, J. Colloid Interface Sci. 534 (2019) 239–247.

[71] S. Xun, C. Wu, L. Tang, et al., One-pot in-situ synthesis of coralloid supported VO_2 catalyst for intensified aerobic oxidative desulfurization, Chin. J. Chem. Eng. 56 (2023) 136–140.

[72] C. Hu, S. Xun, D. Liu, et al., Phosphotungstic acid ionic liquid for efficient photocatalytic desulfurization: synthesis, application and mechanism, Chin. J. Chem. Eng. (2024), https://doi.org/10.1016/j.cjche.2024.02.002.

[73] X. An, L. Xu, L. Xu, et al., Boosting catalytic oxidative desulfurization performance over yolk-shell nickel molybdate fabricated by defect engineering, Inorg. Chem. 62 (2023) 9199–9208.

[74] S. Xun, R. Le, C. Hu, et al., Ionic liquid promotes high dispersion of V_2O_5 on 3D porous g-C_3N_4 carrier to enhance catalytic oxidative desulfurization performance, Energy Fuels 37 (2023) 6276–6280.

[75] J. Yin, W.D. Fu, J.R. Zhang, et al., UiO-66(Zr)-based porous ionic liquids for highly efficient extraction coupled catalytic oxidative desulfurization, Chem. Eng. J. 470 (2023) 144290.

[76] Z. Sun, X. Yang, X. Yu, et al., Surface oxygen vacancies of Pd/Bi_2MoO_{6-x} acts as "electron bridge" to promote photocatalytic selective oxidation of alcohol, Appl. Catal., B 285 (2021) 119790.

[77] H.M. Chen, C.K. Chen, C.J. Chen, et al., Plasmon inducing effects for enhanced photoelectrochemical water splitting: X-ray absorption approach to electronic structures, ACS Nano 6 (2012) 7362–7372.